

## Structural and electrochemical properties of $\text{LiMn}_{1-x}\text{Cr}_x\text{O}_2$ cathode for enhanced lithium-ion battery

N. A. Hassan, M. H. Al-Timimi\*

*Department of Physics, College of Science, University of Diyala, Iraq*

In this study, the urea technique was used to synthesis  $\text{LiMn}_{1-x}\text{Cr}_x\text{O}_2$  powders ( $x = 0, 0.125, 0.25, 0.375, 0.5, 0.625, 0.75$ ). XRD, FTIR, FE-SEM, and EDX studies were used to examine the surface morphology and crystal structure of the produced powders. Both the prepared  $\text{LiMnO}_2$  phase's XRD pattern and X-ray diffraction show that the crystal structure of the  $\text{LiMnO}_2$  phase has a hexagonal shape. When Cr is doped, a cubic  $\text{LiMnO}_2$  nanostructure forms.  $\text{LiMnO}_2$  and  $\text{LiMn}_{1-x}\text{Cr}_x\text{O}_2$  FTIR spectra analysis showed a number of vibrational modes, including (C=O and O-H). According to the FE-SEM data, every sample has a nanostructure. The presence of transition metals (Mn) in  $\text{LiMnO}_2$  and transition metals (chromium and manganese) in  $\text{LiMn}_{1-x}\text{Cr}_x\text{O}_2$  is shown by the EDX spectrum's dimensions.

(Received December 17, 2024; Accepted February 13, 2025)

*Keywords:*  $\text{LiMnO}_2$ , Structure, Morphology, Electrochemical properties, Lithium-ion batteries

### 1. Introduction

Lithium-ion batteries (LIBs) are frequently found in electric cars and portable electronics, innovations in a number of fields. Because of their versatility, high energy ( $\text{W h kg}^{-1}$ ), power densities ( $\text{W kg}^{-1}$ ), and extended cycle life, including electrode materials, cell design, and manufacturing procedures, are necessary to create LIBs with high specific power densities and extended cycle lifetimes. [1, 2]. Lithium-ion batteries (LIBs) were developed to meet the basic needs of emerging technologies. The electrochemical reactions between the battery components control the storage and release of electrical energy. By studying these mechanisms, researchers can gain insight into factors that affect battery performance, such as capacity, efficiency, and cycle life; these properties play a vital role in determining the overall performance of the battery by studying the crystal structure, particle size, and surface morphology of the electrode materials [1-3]. In addition to the structural properties, the electrochemical behavior of batteries is paramount in studying the battery's performance during charge and discharge cycles, its ability to hold over time, and its ability to rate. Electrochemical reactions, such as cyclic voltammetry, galvanic charge-discharge, and electrochemical impedance spectroscopy, are used to analyze the electrochemical properties of LIBs and give valuable information about the battery energy storage capacity, efficiency, and stability under different operating conditions [4, 5].

$\text{LiMnO}_2$ 's distinct electronic structure and redox activity make it an intriguing chemical with a lot of potential. In order to fully utilize  $\text{LiMnCrO}_2$ , nanostructures must be created because they have better qualities than their bulk counterparts. With an emphasis on the synthesis processes and uses of  $\text{LiMnO}_2$  nanostructures, this review outlines the importance of nano materials. Because of their high surface area-to-volume ratio and quantum confinement effects, nanomaterials have unique mechanical, chemical, and physical characteristics. For a variety of uses, such as energy storage, catalysis, sensing, and medicinal applications, these characteristics make them extremely appealing [6, 7].

$\text{LiMnO}_2$  nanostructures can be created using a variety of synthesis techniques, each of which has unique benefits in terms of control over size, shape, and crystallinity. These techniques

---

\* Corresponding author: muhammادتimimi@yahoo.com

<https://doi.org/10.15251/JOR.2025.211.139>

include chemical vapor deposition (CVD), Urea route methods, template-assisted methods, and solvothermal/hydrothermal synthesis. In solvothermal/hydrothermal synthesis, precursor liquids are reacted with at high pressure and temperature to produce distinct nanostructures. Urea route techniques enable easy compositional adjustment and adding, as well as flexibility in precursor selection. Template-assisted methods give the produced nanostructures certain morphologies by using sacrificial templates.  $\text{LiMnO}_2$  nanostructures with the required characteristics for specific applications can be created by adjusting the synthesis conditions and precursor chemistry.

An important aspect of this research is understanding the basic principles and working mechanisms of LIBs. This research focuses on studying lithium-ion batteries' structural and electrochemical properties (LIBs). The structural properties of LIBs refer to the composition, shape, and arrangement of battery components, including electrodes, electrolytes, and separators [8-10].

## 2. Experimental part

The raw materials needed to manufacture cathode materials using the urea route (the molecular formula  $\text{NH}_2\text{CO.NH}_2$ ), with a mass of 60.06 g/mol, citric acid (mass of 192.13 g/mol), nitric acid ( $\text{HNO}_3$ , 70%), lithium chloride ( $\text{LiCl}$ , MW = 42.39), chromium chloride hexahydrate ( $\text{CrCl}_3\cdot 6\text{H}_2\text{O}$ , MW = 266.45 g/mol), and manganese chloride tetrahydrate ( $\text{MnCl}_2\cdot 4\text{H}_2\text{O}$ , MW = 197.90 g/mol). by utilizing stoichiometric quantities of chromium chloride ( $\text{CrCl}_3\cdot 6\text{H}_2\text{O}$ ), manganese chloride ( $\text{MnCl}_2\cdot 4\text{H}_2\text{O}$ ), and lithium chloride ( $\text{LiCl}$ ). as a lithium-ion precursor. These precursors should be carefully blended and constantly swirled after being fully dissolved in distilled water to start the process. . To create a beginning solution (100 mL), the first solution was continuously mixed and supplemented with an aqueous solution made up of citric acid ( $\text{C}_6\text{H}_8\text{O}_7$ ) and urea ( $\text{NH}_2\text{CO.NH}_2$ ). The molar ratio of citric acid was 1:2 in order to preserve metal ion equilibrium. On the other hand, urea's molar ratio to total metal ions was set at 1:1. Finally, nitric acid ( $\text{HNO}_3$ ) was added to the starting solution at a volumetric ratio of 1:0.1 while being continuously stirred. To get rid of the water, the solution was heated to  $85^\circ\text{C}$  for four hours while being constantly agitated.

As the viscosity rose, the solution gradually turned into a dark green resin with sporadic foaming. Evaporation was eventually halted and a dark green gel was produced. After that, the resin was dried for six hours at  $180^\circ\text{C}$  in an oven. As the gel volume increases three to four times above its starting size, intermediary chemicals known as polymerization intermediates are created. Figure 1 shows the steps involved in preparation (a-solution, b-gel, c-foam), followed by four hours of heating at  $800^\circ\text{C}$ .

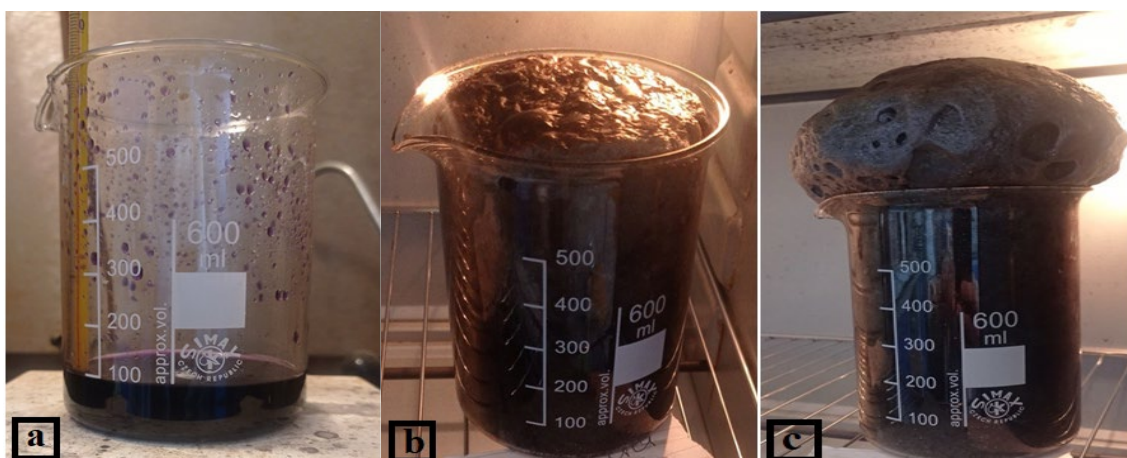


Fig. 1. The preparation process steps (a- solution, b- gel, c- foam).

### 3. Results and discussion

#### 3.1. X-ray Diffraction (XRD)

Using a diffractometer (Shimadzu XRD-6000 powder) XRD test was performed to examine the type of crystal structure and crystal size of the prepared samples. Figure 2 displays the XRD patterns of  $\text{LiMn}_{1-x}\text{Cr}_x\text{O}_2$  nano particle prepared with dissimilar content of chromium metal (0, 0.125, 0.25, 0.375, 0.5, 0.625, and 0.75) to manganese metal (Mn:Cr). The peaks detected at ( $2\theta= 18.27^\circ, 35.36^\circ, 36.99^\circ, 42.98^\circ, 47.05^\circ, 56.83^\circ, 62.4^\circ, 65.61^\circ, 74.81^\circ, 78.78^\circ$ ) of the crystalline planes (111) (311) (222) (400) (331) (511) (440) (531) (222) (444), these peaks attributed to cubic- $\text{LiMnO}_2$  with space collection (Fd-3m no.227) and lattice parameters ( $a = b = c = 8.4105\text{\AA}$ ,  $\alpha = \beta = \gamma = 90^\circ$ ) as shown in figure 1(a), which is corresponded to the standard data (ICDD 00-054-0256).

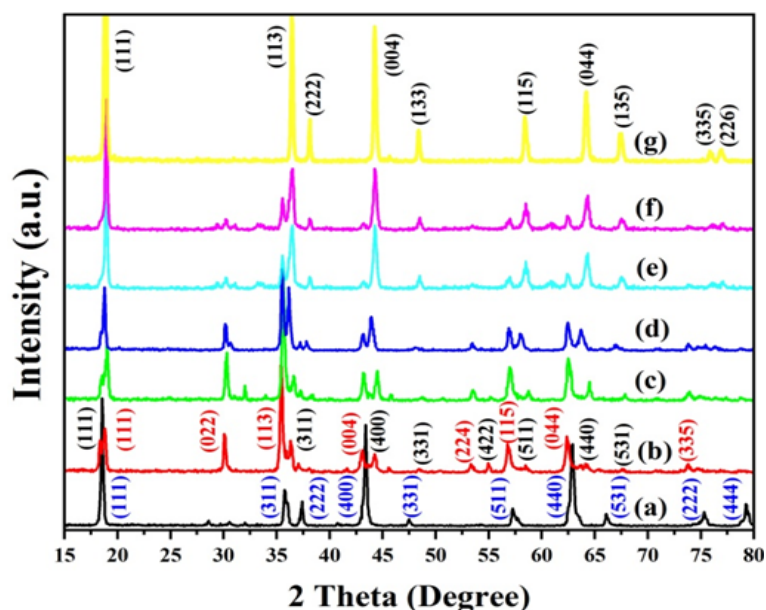


Fig. 2. XRD patterns of prepared  $\text{LiMn}_{1-x}\text{Cr}_x\text{O}_2$  nanopowder at different Cr metal ratio (a)  $\text{LiMnO}_2$  (b)  $\text{LiMn}_{0.875}\text{Cr}_{0.125}\text{O}_2$  (c)  $\text{LiMn}_{0.75}\text{Cr}_{0.25}\text{O}_2$  (d)  $\text{LiMn}_{0.625}\text{Cr}_{0.375}\text{O}_2$  (e)  $\text{LiMn}_{0.5}\text{Cr}_{0.5}\text{O}_2$  (f)  $\text{LiMn}_{0.375}\text{Cr}_{0.625}\text{O}_2$  (g)  $\text{LiMn}_{0.25}\text{Cr}_{0.75}\text{O}_2$ .

When chromium metal is added, observed that there are a difference in the peaks intensity and detected a new peaks, which indicates the entry of chromium ions within the lattice of  $\text{LiMnO}_2$  nanopowder, where the peaks detected at ( $2\theta= 18.75^\circ, 36.35^\circ, 44.2^\circ, 48.41^\circ, 54.88^\circ, 58.52^\circ, 64.29^\circ, 67.2^\circ$ ) of the crystalline planes (111) (311) (400) (331) (422) (511) (440) (531) attributed to the cubic-  $\text{LiMnCrO}_2$  with space group (Fd-3m no.227), ( $a = b = c = 8.1891 \text{\AA}$ ,  $\alpha = \beta = \gamma = 90^\circ$ ) corresponded to the standard data (ICDD 01-088-0608), while the obtained peaks at ( $2\theta= 18.2^\circ, 29.93^\circ, 35.26^\circ, 42.85^\circ, 53.15^\circ, 56.5^\circ, 62.2^\circ, 73.57^\circ$ ) of the crystalline planes (111) (022) (113) (004) (224) (115) (044) (335) assigned to the formation of cubic-  $\text{CrMnO}_2$  with space group (Fd-3m no.227), ( $a = b = c = 8.4350 \text{\AA}$ ,  $\alpha = \beta = \gamma = 90^\circ$ ) agreed with the standard data (ICDD 98-016-7400), as presented in figure 1(b).

From figure 2(c, d, e, f, g), observed that the increase of Cr metal content (0.25, 0.375, 0.5, 0.625, and 0.75) led to the continued slight displacement of the peak's positions with an increase in the peak's intensity. At the Cr metal content (0.75), as presented in figure 2(g), the detected peaks at ( $2\theta= 18.74^\circ, 36.33^\circ, 38^\circ, 44.17^\circ, 48.37^\circ, 58.47^\circ, 64.24^\circ, 67.57^\circ, 76.1^\circ, 77.14^\circ$ ) of the crystalline planes (111) (113) (222) (004) (133) (115) (044) (135) (335) (226) attributed to the formation of pure cubic-  $\text{LiMnCrO}_2$  with space group (Fd-3m no.227), ( $a = b = c = 8.1950 \text{\AA}$ ,  $\alpha = \beta = \gamma = 90^\circ$ ), which agreed with the standard data (ICDD 98-008-4903). On the other hand, with the

increase of Cr metal content the  $\text{MnCrO}_2$  phase decreases until the phase disappeared at the Cr content (0.75). No other impurities peaks have been detected at Cr content (0.75) which indicates a pure cubic- $\text{LiMnCrO}_2$  nanopowder. The XRD spectrum at Cr metal content (0.75) showed clear peaks with high intensity which refers to obtaining a highly crystalline  $\text{LiMnCrO}_2$  phase. The crystalline size of synthesized  $\text{LiMn}_{1-x}\text{Cr}_x\text{O}_2$  at different content of Cr ion was calculated using the most intense peak (111) of  $\text{LiMn}_{1-x}\text{Cr}_x\text{O}_2$  by the Debye–Scherrer's equation, the obtained results demonstrated that the crystalline size of prepared  $\text{LiMnO}_2$  nanopowder is (31.92 nm) and there is a very imperceptible change in crystalline size of  $\text{LiMn}_{1-x}\text{Cr}_x\text{O}_2$  when Cr metal is added (0.125, 0.25, 0.375, 0.5, 0.625, and 0.75), which can be attributed to the chromium ions ( $\text{Cr}^{3+}$ ) substitutes only the manganese ions ( $\text{Mn}^{3+}$ ) because of the close ionic radii ( $\text{Cr}^{3+} = 0.615 \text{ \AA}$  and  $\text{Mn}^{3+} = 0.645 \text{ \AA}$ ) and the same charge in the six-fold coordination [11, 12]. Table 1 presents the XRD calculations of synthesized  $\text{LiMn}_{1-x}\text{Cr}_x\text{O}_2$  samples.

Table 1. The XRD calculations of synthesized  $\text{LiMn}_{1-x}\text{Cr}_x\text{O}_2$  samples.

Sample	2 $\theta$ (deg)	FWHM (deg)	Crystalline size (nm)	(hkl)
$\text{LiMnO}_2$	18.27	0.2456	31.92	(111)
$\text{LiMn}_{0.875}\text{Cr}_{0.125}\text{O}_2$	18.75	0.30382	31.90	(111)
$\text{LiMn}_{0.75}\text{Cr}_{0.25}\text{O}_2$	18.78	0.30219	30.94	(111)
$\text{LiMn}_{0.625}\text{Cr}_{0.375}\text{O}_2$	18.81	0.28467	31.89	(111)
$\text{LiMn}_{0.5}\text{Cr}_{0.5}\text{O}_2$	18.76	0.24878	31.49	(111)
$\text{LiMn}_{0.375}\text{Cr}_{0.625}\text{O}_2$	18.75	0.24878	31.55	(111)
$\text{LiMn}_{0.25}\text{Cr}_{0.75}\text{O}_2$	18.74	0.2305	30.99	(111)

### 3.2. Fourier transforms Infrared Spectroscopy (FT-IR)

The Fourier-transform Infrared spectroscopy FT-IR exam achieved in order to distinguish the functional groups within the samples structure. Figure 3 presents the FTIR spectra of prepared  $\text{LiMn}_{1-x}\text{Cr}_x\text{O}_2$  nanopowder at different Cr content calculated at temperature (800 °C). The obtained FTIR results indicated there are specific characteristic vibration bands of all the prepared  $\text{LiMn}_{1-x}\text{Cr}_x\text{O}_2$  samples.

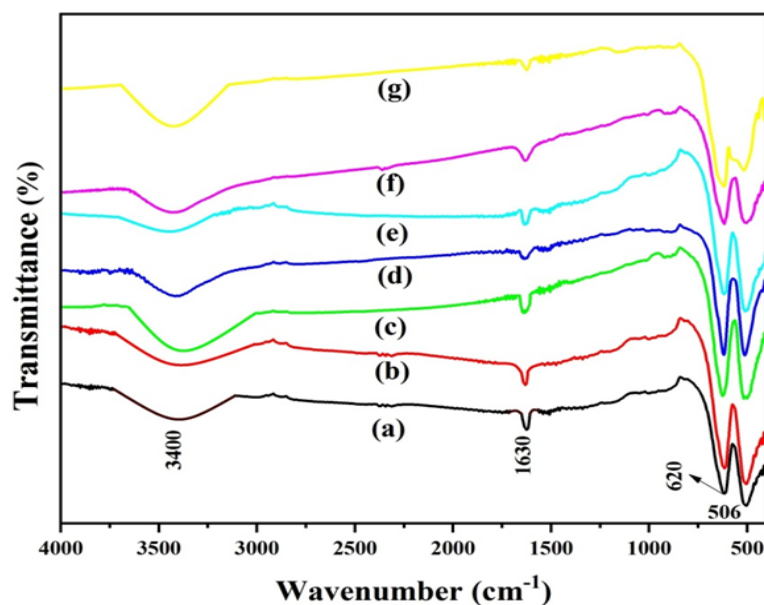


Fig. 3. FT-IR spectra of prepared  $\text{LiMn}_{1-x}\text{Cr}_x\text{O}_2$  nanopowder at different Cr metal ratio (a)  $\text{LiMnO}_2$  (b)  $\text{LiMn}_{0.875}\text{Cr}_{0.125}\text{O}_2$  (c)  $\text{LiMn}_{0.75}\text{Cr}_{0.25}\text{O}_2$  (d)  $\text{LiMn}_{0.625}\text{Cr}_{0.375}\text{O}_2$  (e)  $\text{LiMn}_{0.5}\text{Cr}_{0.5}\text{O}_2$  (f)  $\text{LiMn}_{0.375}\text{Cr}_{0.625}\text{O}_2$  (g)  $\text{LiMn}_{0.25}\text{Cr}_{0.75}\text{O}_2$ .

Metal-oxide bonds (Mn-O and Cr-O) are responsible for the detected peaks at  $506\text{ cm}^{-1}$  and  $620\text{ cm}^{-1}$ . The peaks within the wavenumber range ( $400\text{ to }800\text{ cm}^{-1}$ ) are caused by the stretching vibrations of metal-oxide bonds, while the symmetric (Mn-O) stretching vibrations of octahedral  $\text{MnO}_6$  can be attributed to the strong band  $620\text{ cm}^{-1}$ , while the (Cr-O) stretching vibrations within the  $\text{LiMn}_{1-x}\text{Cr}_x\text{O}_2$  structure are responsible for the peak at  $506\text{ cm}^{-1}$  [13-15]. As shown in figure 1, the discovered broad band centered around  $3400\text{ cm}^{-1}$  is attributed to the asymmetric stretching vibrations of the lattice (-OH) bond due to the absorbed water [15-17], while the peak around  $1630\text{ cm}^{-1}$  is attributed to the bending vibrations of the hydroxide bond (-OH). The results revealed that there is a little change in the FTIR peaks intensity when adding and increase the Cr ions content within the  $\text{LiMnO}_2$  structure, which is assigned to increase the exchange degree of Mn and Cr ions replacement [18].

### 3.3. Field Emission - Scanning Electron Microscopy (FE-SEM)

The surfaces morphology of synthesized  $\text{LiMn}_{1-x}\text{Cr}_x\text{O}_2$  powders investigated using scanning electron microscopy (FEI INSPECT F50), with accelerating voltage of (20 kV). Figures 4 present the FESEM images of synthesized  $\text{LiMn}_{1-x}\text{Cr}_x\text{O}_2$  powders respectively at different scales ( $5\text{ }\mu\text{m}$  and  $500\text{ nm}$ ).

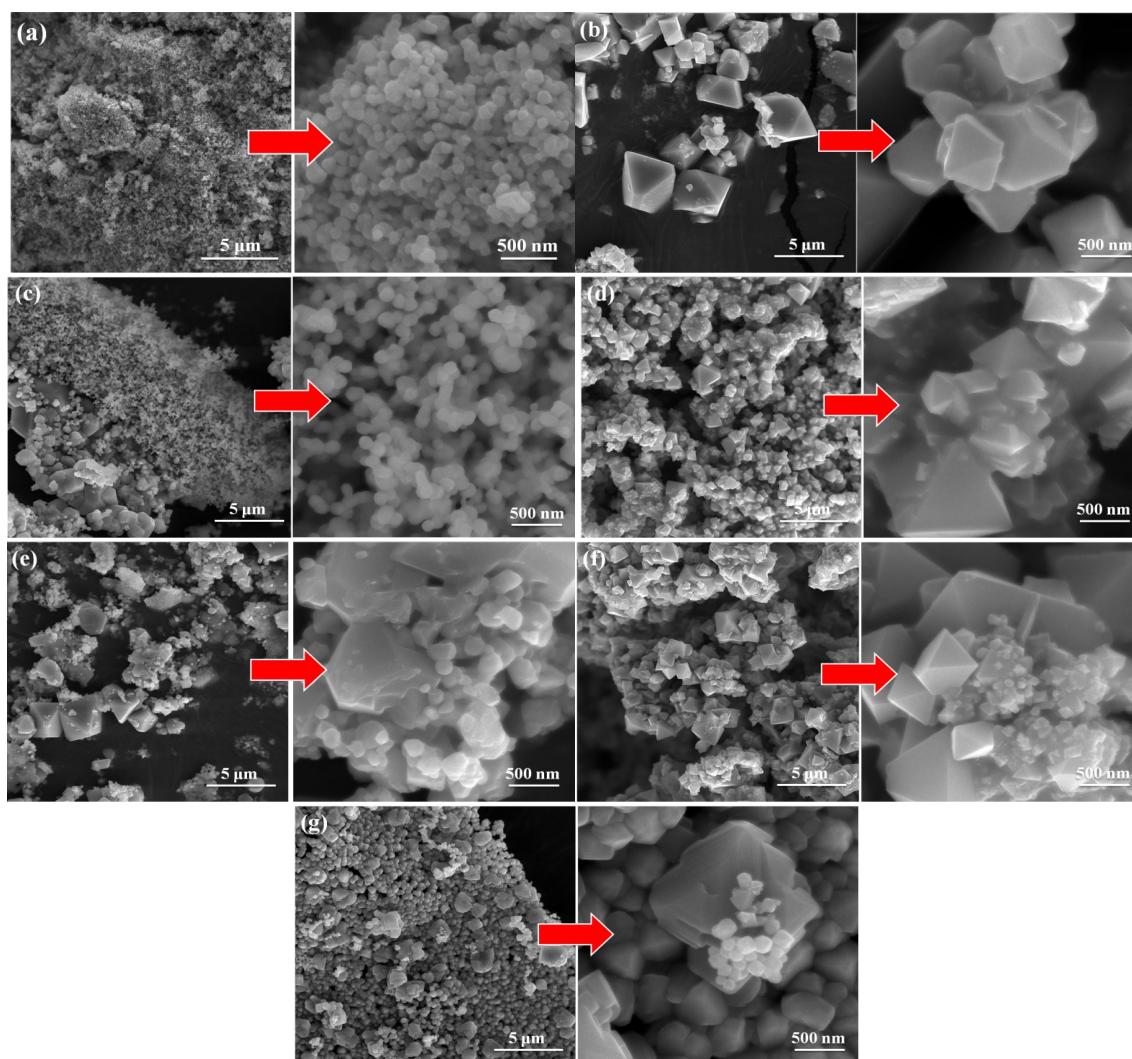


Fig. 4. FESEM images of prepared  $\text{LiMn}_{1-x}\text{Cr}_x\text{O}_2$  nanopowder at different Cr ratio (a) Pure  $\text{LiMnO}_2$  (b)  $\text{LiMn}_{0.875}\text{Cr}_{0.125}\text{O}_2$  (c)  $\text{LiMn}_{0.75}\text{Cr}_{0.25}\text{O}_2$  (d)  $\text{LiMn}_{0.625}\text{Cr}_{0.375}\text{O}_2$  (e)  $\text{LiMn}_{0.5}\text{Cr}_{0.5}\text{O}_2$  (f)  $\text{LiMn}_{0.375}\text{Cr}_{0.625}\text{O}_2$  (g)  $\text{LiMn}_{0.25}\text{Cr}_{0.75}\text{O}_2$ .

The size and morphology of pure  $\text{LiMnO}_2$  sample presented in figure 4(a), the pure  $\text{LiMnO}_2$  composed of uniform semi-spherical like morphology with average particle size about (65 nm). The FESEM images indicated that when the  $\text{LiMnO}_2$  nanoparticles doped with Cr metal at different ratio (0, 0.125, 0.25, 0.375, 0.5, 0.625 and 0.75), the  $\text{LiMn}_{1-x}\text{Cr}_x\text{O}_2$  nanoparticles transformed to semi-cubic like morphology with higher average particle size is between (70 – 90 nm) compared with the pure  $\text{LiMnO}_2$ , where the previous studies revealed that the increasing of Cr concentration within the nanostructure leads to increase the particle size, as presented in figure 4(a, b, c, d, e, f, g) [19].

The FESEM images of prepared  $\text{LiMn}_{1-x}\text{Cr}_x\text{O}_2$  samples showed porous structures of all samples as a result of releasing a huge gases from the reactant substances during the combustion period, the combustion reactions (nitric acid, citric acid and metal salts) primarily compose of metal-ligand complexes formation, which leads to produce flaming or non-flaming results depend on the fuel nature [20, 21].

### 3.4. X-ray energy dispersive spectroscopy (EDX)

The EDX test was accomplished in order to specify the elements composition ratio based on the characteristic peaks for each element inside the samples under testing by the incident electron beam [22]. The synthesized  $\text{LiMn}_{1-x}\text{Cr}_x\text{O}_2$  EDX spectra, including the characteristic elements peaks of each sample, are displayed in figures 1 and 2. Table 2 displays the weight and atomic ratio values of the synthesized samples. Several distinctive peaks of the manganese Mn and oxygen O elements with weight ratios (Mn = 31.82 weight percent, O = 68.18 weight percent) were visible in the obtained EDX spectra of  $\text{LiMn}_{1-x}\text{Cr}_x\text{O}_2$  (at Cr ratio 0). However, new characteristic peaks attributed to the chromium element Cr at weight ratio (Cr = 13.43 weight percent) emerged after adding Cr (at ratio 0.125). As seen in figure 5 and table 2, the findings obtained showed that the weight (%) and atomic (%) values of the Cr element grew as the Cr content increased, while the Mn element decreased. These results were in good agreement with the recommended manganese and chromium content during preparation. The FESEM and XRD data are in good agreement with the  $\text{LiMn}_{1-x}\text{Cr}_x\text{O}_2$  EDX spectra. There are no additional impurity peaks seen in the obtained EDX spectra.

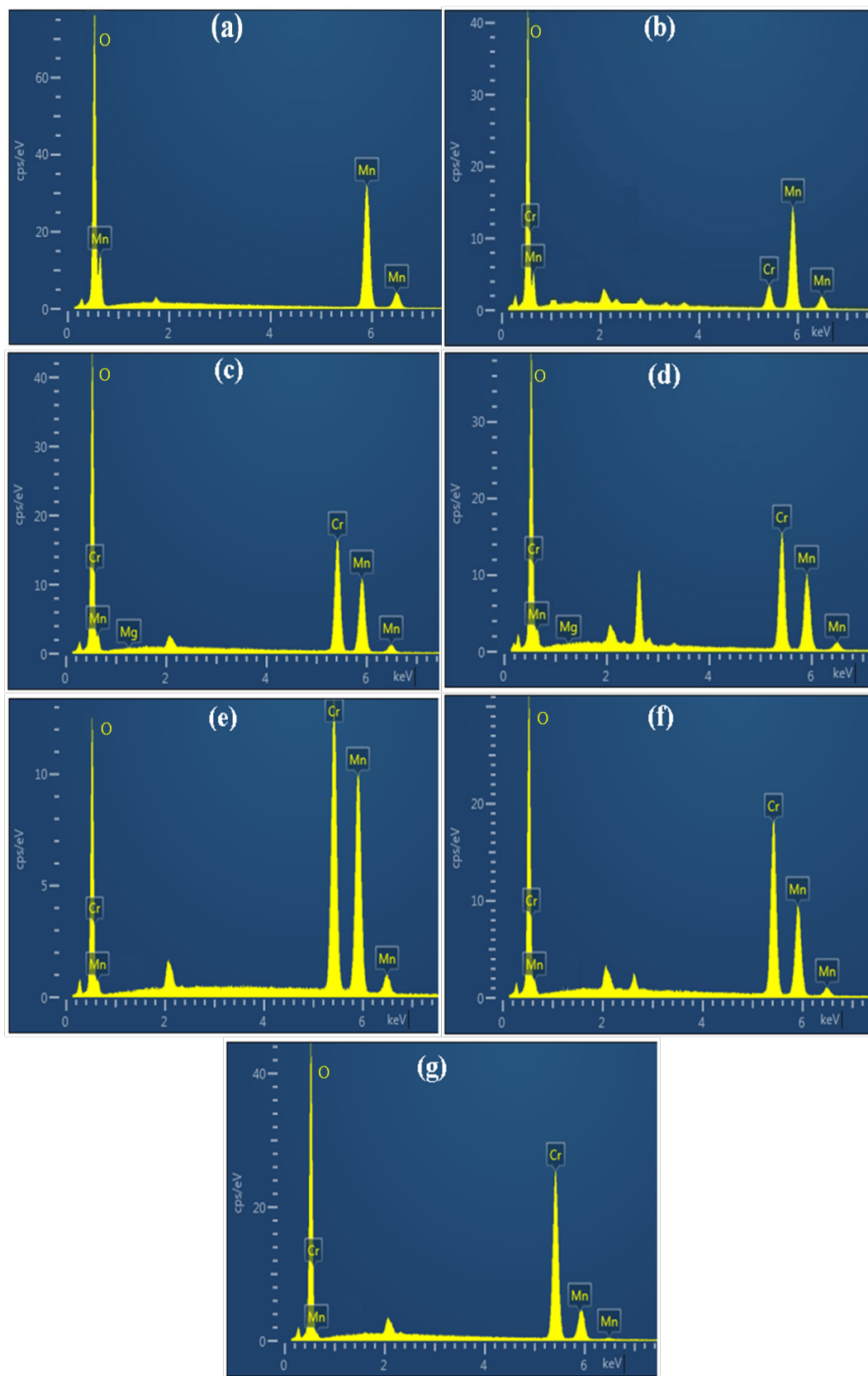


Fig. 5. EDX spectra of prepared  $\text{LiMn}_{1-x}\text{Cr}_x\text{O}_2$  nanopowder at different Cr ratio (a) Pure  $\text{LiMnO}_2$  (b)  $\text{LiMn}_{0.875}\text{Cr}_{0.125}\text{O}_2$  (c)  $\text{LiMn}_{0.75}\text{Cr}_{0.25}\text{O}_2$  (d)  $\text{LiMn}_{0.625}\text{Cr}_{0.375}\text{O}_2$  (e)  $\text{LiMn}_{0.5}\text{Cr}_{0.5}\text{O}_2$  (f)  $\text{LiMn}_{0.375}\text{Cr}_{0.625}\text{O}_2$  (g)  $\text{LiMn}_{0.25}\text{Cr}_{0.75}\text{O}_2$ .

Table 2. The chemical elements ratio of prepared  $\text{LiMn}_{1-x}\text{Cr}_x\text{O}_2$  nanopowder at different Cr ratios.

$\text{LiMn}_{1-x}\text{Cr}_x\text{O}_2$	Element	Weight (%)	Atomic (%)
$\text{LiMnO}_2$	O	31.82	32.84
	Mn	68.18	67.16
	<b>Total</b>	<b>100.00</b>	<b>100.00</b>
$\text{LiMn}_{0.875}\text{Cr}_{0.125}\text{O}_2$	O	33.14	35.74
	Mn	53.43	49.12
	Cr	13.43	15.14
	<b>Total</b>	<b>100.00</b>	<b>100.00</b>
$\text{LiMn}_{0.75}\text{Cr}_{0.25}\text{O}_2$	O	35.6	33.81
	Mn	49.22	48.88
	Cr	15.18	17.31
	<b>Total</b>	<b>100.00</b>	<b>100.00</b>
$\text{LiMn}_{0.625}\text{Cr}_{0.375}\text{O}_2$	O	37.14	36.63
	Mn	39.55	42.31
	Cr	23.31	21.06
	<b>Total</b>	<b>100.00</b>	<b>100.00</b>
$\text{LiMn}_{0.5}\text{Cr}_{0.5}\text{O}_2$	O	38.21	40.15
	Mn	31.24	32.11
	Cr	30.55	27.74
	<b>Total</b>	<b>100.00</b>	<b>100.00</b>
$\text{LiMn}_{0.375}\text{Cr}_{0.625}\text{O}_2$	O	36.91	36.45
	Mn	24.2	22.3
	Cr	38.89	41.25
	<b>Total</b>	<b>100.00</b>	<b>100.00</b>
$\text{LiMn}_{0.25}\text{Cr}_{0.75}\text{O}_2$	O	37.88	35.89
	Mn	12.91	11.56
	Cr	49.21	52.46
	<b>Total</b>	<b>100.00</b>	<b>100.00</b>

### 3.5. The cyclic voltammetry (CV)

This technique is used to determine the electrochemical elements influencing the battery voltage and its reversibility. The battery's oxidation and reduction reaction processes are examined using this technique, which also helps to comprehend the electron diffusion process and its catalysts. Cyclic voltammetry (CV) is carried out by measuring the current that results from cycling the working electrode's potential [23].

Figure (6) shows the CV curve at sintering temperatures of 800°C. From the figure we notice that the range of efforts starts from (2.0 V) and ends at (4.8 V) at sintering temperatures (800 degrees Celsius), and then this range is reversed, Broad anodic peaks located at (4.017 and 4.178 V) for sample a)  $\text{LiMn}_{0.875}\text{Cr}_{0.125}\text{O}_2$  and (4.05 and 4.175 V) for sample b)  $\text{LiMn}_{0.25}\text{Cr}_{0.75}\text{O}_2$  were observed at sintering temperatures of 800 °C).

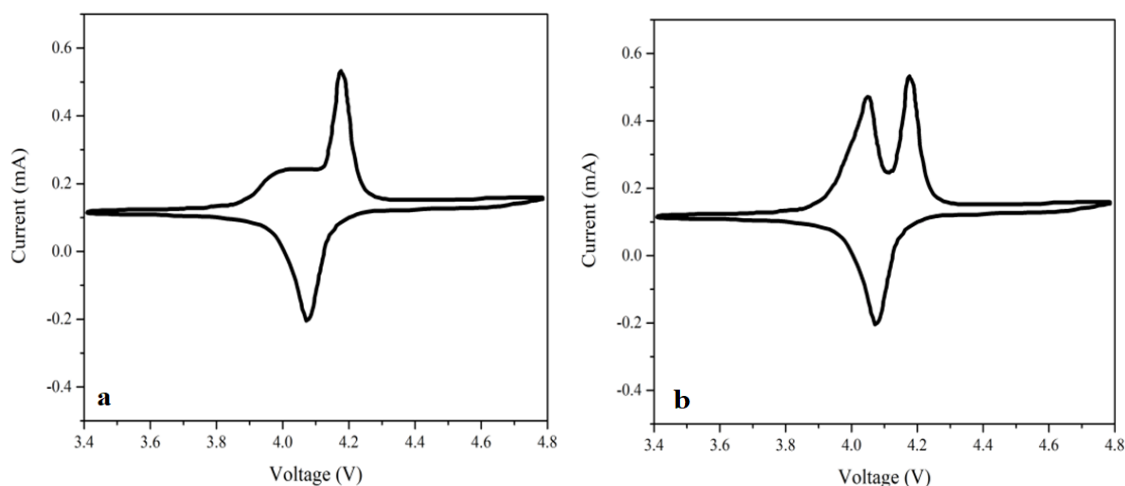


Fig. 6. The CV results for a)  $\text{LiMn}_{0.875}\text{Cr}_{0.125}\text{O}_2$ , b)  $\text{LiMn}_{0.25}\text{Cr}_{0.75}\text{O}_2$  sample.

It appears from Figure (6) that sample (b) has witnessed a shift of the anodic peak towards lower voltage. This indicates that the sample has better kinetic energy than the other sample due to the elimination of lithium-ion intercalation. The redox zone is represented by the anodic and cathodic peaks, respectively. The cathodic peaks also appeared at (4.076) for sample a)  $\text{LiMn}_{0.875}\text{Cr}_{0.125}\text{O}_2$ , and cathodic peaks appeared at (4.072) for sample b)  $\text{LiMn}_{0.25}\text{Cr}_{0.75}\text{O}_2$ . sample at  $800^\circ\text{C}$ ) annealing temperature.

It was found that the cathodic peaks shift towards the higher voltage and are the most shifted, and this indicates that they have a high lithium-ion diffusion mobility at an annealing temperature of  $800^\circ\text{C}$ . This result is consistent with (Song Huanqiao et al.) [24].

### 3.6. Charge and discharge

Battery charging and discharging were studied using a Neware multi-channel CT-3008, and it was found that when the battery discharge curve is fairly constant, it means that the battery voltage remains constant throughout the battery discharge cycle, which often requires complex setup methods to achieve this. If the battery discharge curve slopes downward, this means that the battery does not maintain its voltage stably during the battery discharge cycle, and this type of battery requires an increase in its size to support high power applications at the end of the discharge cycle [23].

In Figure (7), the voltage range between 3.8 and 4.3 V gradually decreases before becoming stable at 3.8 V, where the capacity is nearly constant. We observe a significant drop in capacity after the voltage (3.8 V), and the discharge cut-off point was 3V. This relates to  $\text{LiMn}_{0.875}\text{Cr}_{0.125}\text{O}_2$  sample a). The voltage range for sample b)  $\text{LiMn}_{0.25}\text{Cr}_{0.75}\text{O}_2$  decreases between 4.1-4.4 V, and stability follows a significant drop in capacity. The cut-off point is at 3 V.

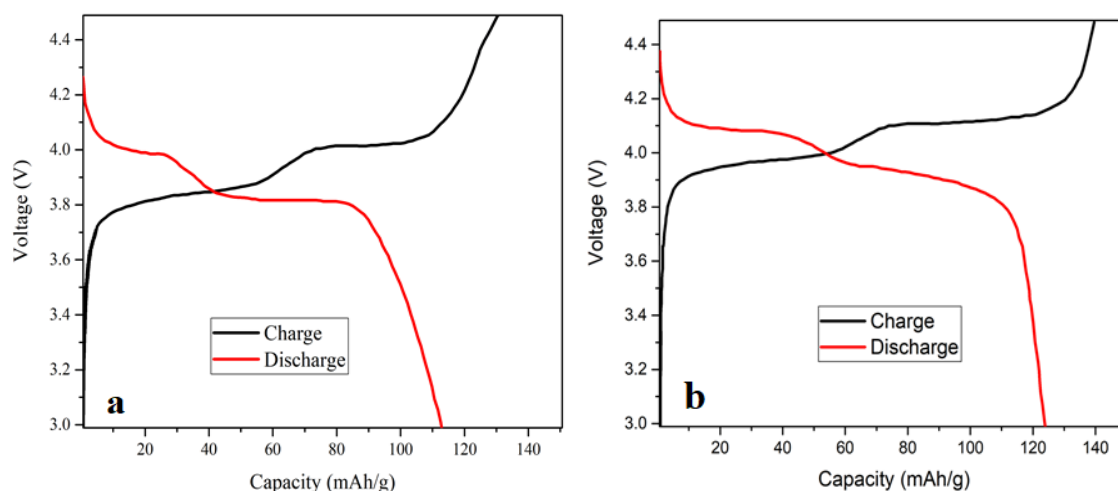


Fig. 7. The charge curve for a)  $\text{LiMn}_{0.875}\text{Cr}_{0.125}\text{O}_2$ , b)  $\text{LiMn}_{0.25}\text{Cr}_{0.75}\text{O}_2$  sample.

### 3.7. Electrochemical impedance spectroscopy (EIS).

A powerful method for examining a cell's impedance characteristics is electrochemical impedance spectroscopy (EIS), which employs a tiny amplitude alternating current signal. To create an impedance spectrum for the electrochemical cell being tested, the ac signal is scanned across a broad frequency range. An electrical circuit that is regarded as an equivalent model is compared to the EIS data in order to analyze it. are among the most popular techniques for providing adequate details regarding the electrochemical performance of the materials. EIS analyses were carried out to distinguish between samples processed at  $800^\circ\text{C}$ , as seen in figure (8). For four hours at  $0.2\text{ V}$ , EIS measurements were conducted in a charged condition. A graphite sheet served as the counter and saturated calomel as the reference electrode.

EIS is produced at a sintering temperature of ( $800^\circ\text{C}$ ). At this temperature, we find a decrease in the diameter of the semicircle, and it is also noted that the height of the semicircle from the axis of the real part of the impedance increases at this temperature.

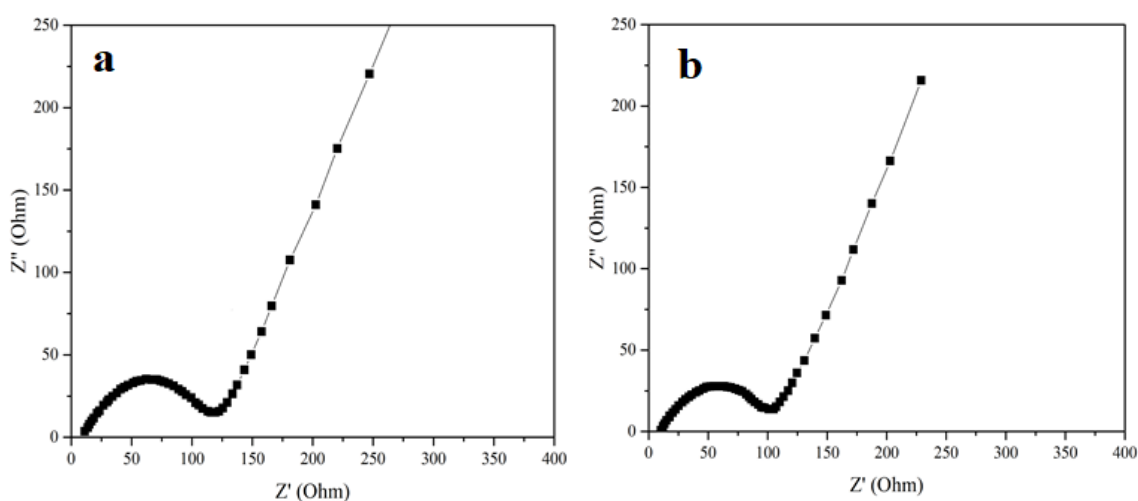


Fig. 8. EIS for a)  $\text{LiMn}_{0.875}\text{Cr}_{0.125}\text{O}_2$ , b)  $\text{LiMn}_{0.25}\text{Cr}_{0.75}\text{O}_2$  sample.

#### 4. Conclusion

LiMn<sub>1-x</sub>Cr<sub>x</sub>O<sub>2</sub> nanoparticles were synthesized in this study by the urea technique and then calcined for four hours at 800 °C. The produced LiMnO<sub>2</sub> nanostructures' crystal size was successfully decreased by the addition of Cr metal. These nanostructures have a large surface area, short diffusion routes for electron and lithium-ion transfer, and improved structural stability, according to characterization experiments. Even in the face of volume changes during cycling, these characteristics allow the electrodes to retain greater capacitance, enhanced capacity, and superior cycling stability as compared to their bulk counterparts.

It was verified that the nanoparticles' crystalline diameters fell within the nanometer range. Field emission scanning electron microscopy (FE-SEM) showed that all samples had nanometer-scale dimensions, while Fourier-transform infrared (FT-IR) spectroscopy shed light on the chemical bonds found in the produced materials. The elemental makeup of the composite materials was further confirmed by energy-dispersive X-ray spectroscopy (EDX). Interestingly, the structural and electrochemical characteristics of the produced materials were significantly influenced by the addition of Cr. Our knowledge of the material's characteristics and possible uses in energy storage, catalysis, and other cutting-edge sectors has been greatly improved by these discoveries.

#### References

- [1] K. Kariatsumari, H. Kume, H. Yomogita, P. Keys, Nikkei Electronics Asia, ed: February, 2010.
- [2] M. Abdullah, H. Hasan, M. Al-Timimi, W. Albanda, M. Alhussainy, M. Dumitru, Journal of Ovonic Research Vol, vol. 15, no. 3, pp. 199-204, 2019.
- [3] H. Homada, N. Alia, O. Al-Jubourib, M. Al-Timimia, Journal of Ovonic Research, vol. 19, no. 6, pp. 783-791, 2023; <https://doi.org/10.15251/JOR.2023.196.783>
- [4] B. Deng, H. Nakamura, M. Yoshio, Journal of power sources, vol. 180, no. 2, pp. 864-868, 2008; <https://doi.org/10.1016/j.jpowsour.2008.02.071>
- [5] R. Thirunakaran, A. Sivashanmugam, S. Gopukumar, C. W. Dunnill, D. H. Gregory, Journal of Physics and Chemistry of Solids, vol. 69, no. 8, pp. 2082-2090, 2008; <https://doi.org/10.1016/j.jpcs.2008.03.009>
- [6] H. Al-Rikabi, M. Al-Timimi, W. Albanda, Digest Journal of Nanomaterials & Biostructures (DJNB), vol. 17, no. 3, 2022; <https://doi.org/10.15251/DJNB.2022.173.889>
- [7] H. S. Al-Rikabi, M. H. Al-Timimi, I. K. Abd, AIP Conference Proceedings, 2023, vol. 2834, no. 1: AIP Publishing; <https://doi.org/10.1063/5.0176417>
- [8] C. Julien, A. Mauger, Ionics, vol. 19, pp. 951-988, 2013; <https://doi.org/10.1007/s11581-013-0913-2>
- [9] C. M. Julien, A. Mauger, K. Zaghbi, H. Groult, Inorganics, vol. 2, no. 1, pp. 132-154, 2014; <https://doi.org/10.3390/inorganics2010132>
- [10] H. Homad, N. Ali, O. Al-Jubouri, M. Al-Timimi, B. Abbas, EUREKA: Physics and Engineering, no. 4, pp. 160-172, 2024; <https://doi.org/10.21303/2461-4262.2024.003310>
- [11] V. Kusigerski, D. Marković, V. Spasojević, N. Cvjetičanin, M. Mitrić, D. Jugović, D. Uskoković, Journal of magnetism and magnetic materials, vol. 320, no. 6, pp. 943-949, 2008; <https://doi.org/10.1016/j.jmmm.2007.09.011>
- [12] A. Hamad, L. Li, Z. Liu, Applied Physics A, vol. 122, pp. 1-15, 2016; <https://doi.org/10.1007/s00339-016-0426-8>
- [13] M. Abdullah, M. Al-Timimi, W. Albanda, M. Dumitru, A. Balan, C. Ceaus, I. Stamatina, Digest Journal of Nanomaterials and Biostructures, vol. 14, no. 4, pp. 1179-1193, 2019.
- [14] Q. Feng, Y. Miyai, H. Kanoh, K. Ooi, Chemistry of materials, vol. 5, no. 3, pp. 311-316, 1993; <https://doi.org/10.1021/cm00027a013>

- [15] Y. Zhang, W. Li, L. J. France, Z. Chen, Q. Zeng, D. Guo, X. Li, ACS omega, vol. 4, no. 5, pp. 8681-8692, 2019; <https://doi.org/10.1021/acsomega.9b00445>
- [16] M. Helan, L. J. Berchmans, Materials and Manufacturing Processes, vol. 26, no. 11, pp. 1369-1373, 2011; <https://doi.org/10.1080/10426914.2010.536932>
- [17] M. W. Raja, S. Mahanty, P. Ghosh, R. N. Basu, H. S. Maiti, Materials research bulletin, vol. 42, no. 8, pp. 1499-1506, 2007; <https://doi.org/10.1016/j.materresbull.2006.11.002>
- [18] J. C. Knight, S. Therese, A. Manthiram, ACS applied materials & interfaces, vol. 7, no. 41, pp. 22953-22961, 2015; <https://doi.org/10.1021/acsami.5b06179>
- [19] L. Li, C. Xiang, X. Liang, B. Hao, Synthetic metals, vol. 160, no. 1-2, pp. 28-34, 2010; <https://doi.org/10.1016/j.synthmet.2009.09.026>
- [20] J. Bai, F. Meng, C. Wei, Y. Zhao, H. Tan, J. Liu, Ceramics-Silikaty, vol. 55, no. 1, pp. 20-25, 2011.
- [21] S. T. Aruna, A. S. Mukasyan, Current opinion in solid state and materials science, vol. 12, no. 3-4, pp. 44-50, 2008; <https://doi.org/10.1016/j.cossms.2008.12.002>
- [22] M. Scimeca, S. Bischetti, H. K. Lamsira, R. Bonfiglio, E. Bonanno, European journal of histochemistry: EJM, vol. 62, no. 1, 2018; <https://doi.org/10.4081/ejm.2018.2841>
- [23] Z. Peng, Q. Jiang, K. Du, W. Wang, G. Hu, Y. Liu, Journal of Alloys and Compounds, vol. 493, 2010; <https://doi.org/10.1016/j.jallcom.2009.12.172>
- [24] H. Song, Y. Liu, C. Zhang, C. Liu, G. Cao, Journal of Materials Chemistry A, vol. 3, no. 7, pp. 3547-3558, 2015; <https://doi.org/10.1039/C4TA05616G>